




Article

Numerical Study of Laminar Flow and Vortex-Induced Vibration on Cylinder Subjects to Free and Forced Oscillation at Low Reynolds Numbers

M. S. Al Manthari ¹, Carlton Azeez ¹, M. Sankar ^{1,*} and B. V. Pushpa ²

¹ College of Computing and Information Sciences, University of Technology and Applied Sciences, Ibra 516, Oman; maimouna.almunthari@utas.edu.om (M.S.A.M.); carlton.aziz@utas.edu.om (C.A.)

² College of Computing and Information Sciences, University of Technology and Applied Sciences, Nizwa 611, Oman; bvpushpa.gowda@gmail.com

* Correspondence: manisankariyer@gmail.com

Abstract: In this study, we aimed to numerically investigate the 2D laminar flow over a cylindrical body and performed vortex-induced vibration analyses on a circular cylinder of unit radius placed in a channel, with the cylinder assumed to be fixed. The cases of a cylinder under forced oscillation and three different scenarios of a freely oscillating cylinder were analyzed. The fluid domain dynamics were governed by the incompressible Navier–Stokes equations; however, the structural field was described using nonlinear elastodynamic equations. Fluid and solid domains were discretized with the finite volume method (FVM) in space and time. Predictions of hydrodynamic forces, namely lift and drag terms, were determined for each scenario. An increase in the Reynolds number caused an exponential increment in the lift force. In the case of a stabilized flow, the collective decrease in stiffness and damping decreased the maximal drag and lift factors. Furthermore, it was noticed that the lift factor was minimally altered by variations in damping and stiffness in comparison with the change in the drag factor. From these observations, it appears that the lift factor probably correlates with the cylinder’s structure and fluid properties.

Keywords: laminar fluid flow; hydrodynamic flow; lift and drag coefficients; OpenFOAM; VIV



Citation: Al Manthari, M.S.; Azeez, C.; Sankar, M.; Pushpa, B.V. Numerical Study of Laminar Flow and Vortex-Induced Vibration on Cylinder Subjects to Free and Forced Oscillation at Low Reynolds Numbers. *Fluids* **2024**, *9*, 175. <https://doi.org/10.3390/fluids9080175>

Academic Editor: Pengtao Yue

Received: 18 May 2024

Revised: 19 July 2024

Accepted: 24 July 2024

Published: 30 July 2024



Copyright: © 2024 by the authors. Licensee MDPI, Basel, Switzerland. This article is an open access article distributed under the terms and conditions of the Creative Commons Attribution (CC BY) license (<https://creativecommons.org/licenses/by/4.0/>).

1. Introduction

Vortex-induced vibration (VIV) refers to motion induced on a bluff body subject to an external fluid flow with periodic irregularities. Due to its significance in technical applications and scholarly investigations, the VIV processes of bluff structures have been investigated in detail. Numerous theoretical and experimental investigations have been carried out on the topic of fluid–solid interaction (FSI), ranging from solid to elastic cylinders, to develop the fundamental physics underlying the analysis results.

Anagnostopoulos [1,2] researched VIV with a numerical approach and investigated VIV behavior in a circular, two-dimensional cylindrical tube with $Re = 200$ and two degrees of freedom (DoF). The incompressible Navier–Stokes equations were resolved in 2D by using the space–time finite element method, while the motion of the cylinder was resolved by using the explicit integral method. The VIV results showed that at low mass damping, the lift and drag coefficients had different trajectories.

Govardhan and Williamson [3] examined the outcome of free oscillations in terms of lift factors as well as near-wake vorticity on a 2D circular cylinder in a distinct experimental study. The study’s conclusions helped to further the knowledge of FSI and the mechanisms controlling body motion, enabling the wake response to motion to be assessed separately. Later, Williamson and Govardhan [4] reported vortex wake states in a different numerical investigation by using earlier predictions. The relationship between free and forced vibrations and the suitability of elastically fixed cylindrical flow for configurations of greater

complexity were the primary research topics in their study. Alterations in the shedding patterns of a freely vibrating cylinder in the in-line and cross-flow directions support the idea that differences in global geometrical responses rely on the cylinder vibrations' orientation [5,6]. The results obtained by Williamson and Jauvtis [5] clearly suggest that high harmonics may contribute to the lift force.

A substantial number of studies on the distribution of VIV are also available [7–12], spanning experimental and theoretical studies, motion with single to multiple DoF, flexible and solid movements, and VIV phenomena in liquid and gas. Because it is simple to employ grids to change a comparatively thicker laminar flow for the associated surface layer in the transition stage, numerical results are typically obtained in the subcritical Re range [13]. It becomes more challenging to resolve the associated turbulence as Re increases to critical as well as supercritical ranges, where the boundary region is comparatively six times smaller than that in the subcritical area [14]. This may be the cause of the lower number of computational fluid dynamics (CFD) investigations on a flow past a cylindrical surface at a larger Re compared with a lower Re . When the vortices around a bluff body are not symmetrically produced, distinct lift and drag factors are created in either region of the structure, which results in movement perpendicular to the direction of flow. This movement alters the eddy formulation in a manner that it results in a constrained motion amplitude. Recently, the FSI phenomenon has attracted interest in wide variety of applications, including energy harvesting [15], offshore pipeline arrangements [16], and many more thrust areas.

Generally, the VIV phenomenon is encountered in hydrodynamic systems where excitation occurs because of the vortex shedding of bluff bodies. The process of vortex shedding creates an asymmetric pressure distribution over a circular cylinder and eventually leads to body movement. The body motion is nonlinear and occurs in a range of frequencies, thus leading to increases in the strength of the shed vorticity. Therefore, this phenomenon can increase body fatigue and cause potential damage [17]. Some interesting and recent studies involving VIV phenomena in flow oscillation or free surface impacts have been reported in the literature [18–23]. However, the forced oscillation condition employs identical principles by considering distinct group variables. For instance, an induced oscillating cylinder maintains identical amplitude oscillation (A/D , with D being the diameter of the cylinder), and the frequency (f_0) changes at specific locations so that the ratio f_0/f_s is unity, where f_0 and f_s represent the natural and oscillation frequencies, respectively. However, there are still some unresolved issues in predicting flow-induced motion based on forced oscillations. Extensive research has been conducted on the shape of wake and forces exerted on a cylinder when it is subjected to forced oscillation [24–27]. It is worth mentioning that the above-cited works mainly lack details to account for the combined impacts of FSI and VIV on stationary and forced oscillating cylinders.

Fluid–solid interaction (FSI) problems are widely analyzed in various engineering fields, e.g., wind-induced vibration phenomena in civil engineering, engineering design in materials science, some internal flow models that require very accurate simulations to achieve very high performance, and blood flow, as an example of FSI in the human body. A review of FSI is important because it enriches knowledge on engineering design to counteract wave stress effects on solids, which may result in large deformation and damage. From an engineering perspective, the effects of wave stress greatly influence solid design and material selection. This systematic and careful literature analysis indicates a lack of understanding of the VIV phenomena in cylindrical structures at low Reynolds numbers. In the current study, we investigated the vortex-induced vibration theory for cylindrical structures. A solution for the free-vibration condition was derived for different cases by considering various constraints.

2. Model Equations

2.1. Fluid Flow Model

In the case of the fluid flow model, a circular cylinder with diameter $D = 1$ m was placed in a channel of length $20D$ and width $8D$. The flow velocity was 1 m/s at the inlet and zero gradient at the outlet. Zero pressure was also set at the outlet. The cylinder was assumed to be fixed, which means that it could not move although it was subjected to some hydrodynamic forces, and its center coordinates were $(0, 0, 0)$. This case was considered a laminar flow case with a Reynolds number equal to 100. Initially, both the solid and fluid domains were in the rest position, and no-slip boundary conditions were implemented for the walls and the fluid–solid interfaces. Moreover, the outlet Neumann conditions were set to zero for both velocity and pressure, and the profile of parabolic velocity was set at the inlet in the flow domain. The static circular cylinder case was considered to be two-dimensional, incompressible, and subject to a horizontally uniform flow. The flow conditions were determined by assuming that the flow occurred in a rectangular channel in which the circular cylinder was symmetrically placed between the two plane walls with the slip boundary conditions represented in Figure 1. The incompressible viscous fluid flow dynamics were governed by the Navier–Stokes equations. The conservation principles of continuity and momentum were modeled with continuity and momentum equations, respectively, which were valid in the entire physical domain as expressed by the following system of partial differential equations:

$$\nabla \cdot \mathbf{U}_f = 0, \tag{1}$$

$$\frac{\partial \mathbf{U}_f}{\partial t} + (\nabla \cdot \mathbf{U}_f) \cdot \mathbf{U}_f = -\frac{\nabla p}{\rho_f} + \nabla \cdot (\nu_f \nabla \mathbf{U}_f), \tag{2}$$

where \mathbf{U}_f is the flow velocity, ρ_f is the density of the fluid, p is the fluid pressure, and $\nu_f = \frac{\mu_f}{\rho_f}$ and μ_f represent kinematic and dynamic viscosities, respectively.

The conservation laws for mass and momentum represented by Equations (1) and (2) were fulfilled in the required domain for fluid $\Omega_{f,0}$. These model equations for fluid flows with a stationary mesh can be discretized by choosing an Eulerian coordinate system with a fixed mesh domain [13]. However, for a Lagrangian description, the mesh must change with the flow. However, these types of procedures cannot be applied to computational regions that change significantly over time. In such cases, the arbitrary Lagrangian–Eulerian (ALE) description [13] is employed for the flow model equations on a deformable mesh, as shown in the subsequent subsections.

2.2. Structure Model

The momentum balance for the chosen structural geometry is given as

$$\frac{\partial^2 (\rho_s U_s)}{\partial t^2} - \nabla \cdot \sigma_s = \rho_s F_b. \tag{3}$$

where U_s and ρ_s represent the solid displacement and density, respectively; F_b denotes the body force; and σ_s indicates the Cauchy stress tensor.

In a similar manner, strain tensor ϵ in the form of U_s is given by

$$\epsilon = \frac{1}{2} [\nabla U_s + (\nabla U_s)^T]. \tag{4}$$

The strain and stress tensors, by Hook’s law, are defined using the reaction below:

$$\sigma_s = 2\mu_s \epsilon + \lambda_s tr(\epsilon) \mathbf{I}. \tag{5}$$

In the above equation, \mathbf{I} denotes the unit matrix, tr represents the trace, μ_s and λ_s are known as Lamé constants and estimate the characteristics of an elastic material. The magni-

tudes of these two constants are connected to the quantities ν_s and E_s , which are Poisson’s ratio and Young’s modulus, respectively, and are defined by the following equations:

$$\lambda_s = \frac{\nu_s E_s}{(1 + \nu_s)(1 - 2\nu_s)} \tag{6}$$

$$\mu_s = \frac{E_s}{2(1 + \nu_s)}. \tag{7}$$

Using the above relations in Equation (3) yields the following:

$$\frac{\partial^2(\rho_s U_s)}{\partial t^2} - \nabla \cdot [\mu_s \nabla U_s + \mu_s (\nabla U_s)^T + Itr(\nabla U_s)] = \rho_s F_b. \tag{8}$$

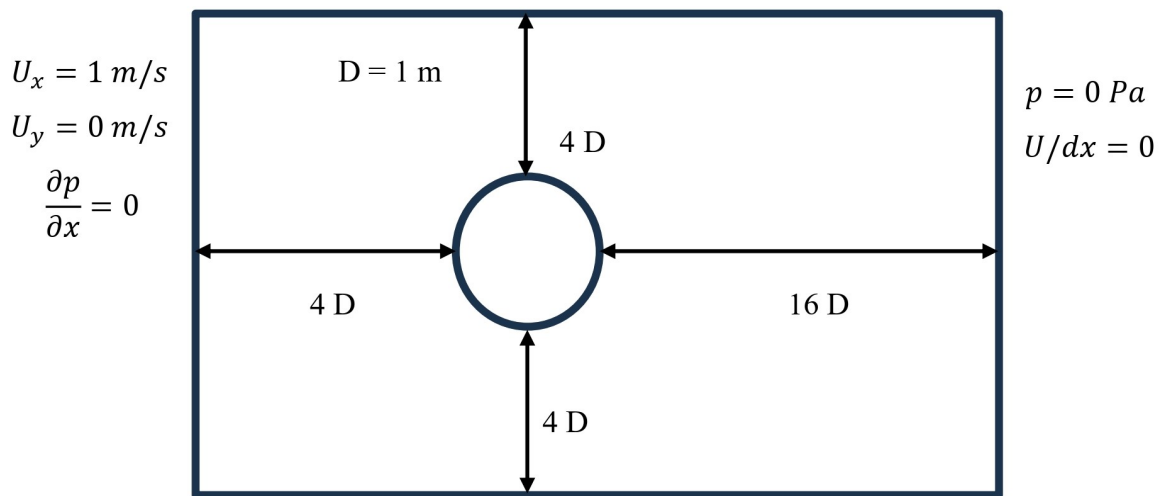


Figure 1. Physical structure and auxiliary conditions.

2.3. Boundary Conditions

The inflow velocity boundary conditions were as follows:

- (i) At the inlet (inflow), uniform flow conditions were assumed, that is, $U_x = U$, $U_y = U_z = 0$.
- (ii) At the outlet (outflow), the flow variables had zero diffusion, which means that the boundary conditions at the outlet were extrapolated from the domain to result in the upstream flow conditions. The velocity and pressure were updated according to the extrapolation at the outflow. This is based on the assumption of a fully developed flow experiencing no change in the area at the outlet boundary [28].

$$\frac{\partial p}{\partial t} + \bar{U}_n \frac{\partial p}{\partial n} = 0$$

- (iii) At the upper and lower walls, where the viscous effects were negligible, boundary slip conditions were assumed.
- (iv) On the cylindrical structure wall, the no-slip condition was applied, according to which all the velocity components on the cylinder surface were zero due to the fluid viscous effects.
- (v) Moreover, the outlet Neumann conditions were set to zero for both velocity and pressure. The above-mentioned conditions are also specified in Figure 1.

2.4. Dimensionless Parameters

Drag, mean drag, and lift coefficients (C_D , \bar{C}_D , and C_L , respectively) are non-dimensional parameters for the drag and lift forces and are formulated as

$$C_D = \frac{F_D}{\frac{\rho}{2}U^2LD}, \bar{C}_D = \frac{\bar{F}_D}{\frac{\rho}{2}U^2LD} \text{ and } C_L = \frac{F_L}{\frac{\rho}{2}U^2LD}$$

where U, D, L , and ρ are the flow velocity, the cylinder diameter, the cylinder length, and the fluid density, respectively.

3. Computational Procedure

The aim of any discretization method is to transform partial differential equations (PDEs) into a system of algebraic expressions. The latter results in a set of values that correspond to the solution of the original equations at some determined locations in space and time. Since OpenFOAM relies upon the finite volume method (FVM) and the discretization discussed in this section adheres to the FV process, the discretization approach of the computational region can be categorized as spatial and temporal discretization [29,30]. Spatial discretization involves partitioning the computational area into a finite quantity of parts, known as control volumes (CVs), which form a mesh that completely occupies the physical configuration. The discretization of the temporal term is exclusively employed for unsteady cases and involves the segmentation of time into discrete intervals known as time steps.

Figure 2 depicts a standard CV with computational point P being positioned in its center, satisfying

$$\int_{V_p} (x - x_p)dV = 0 \tag{9}$$

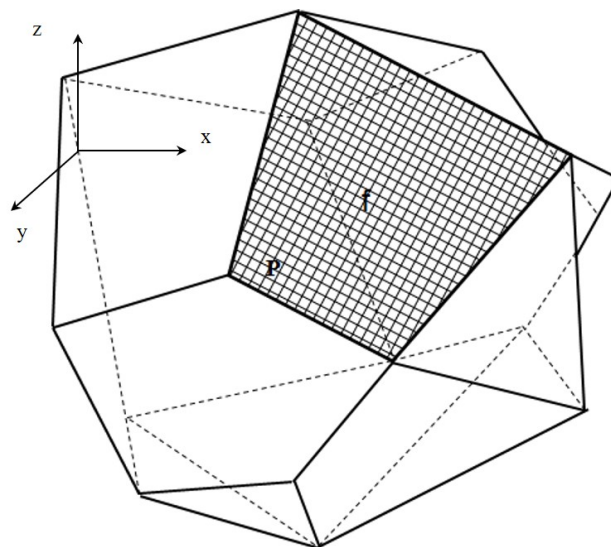


Figure 2. Control volume structure.

In the CVs, cell faces are separated as internal faces between two CVs and border faces, which match the geometry boundaries. For every face, the face area vector extends outwardly from the CV with a bottom label but perpendicular to the face, with the same size as the face area. The owner and neighbor cell centers of the shaded face are designated P and K in Figure 2, respectively, with the vector face area pointing outwardly from cell P . For convenience, all faces of the CVs are indicated by f , which also depicts the center value. In OpenFOAM, variables are mostly retained in the element center, but sometimes on vertices or faces. Prior to obtaining the solutions to the model equations, choosing the domain locations for the variable values is crucial. Figure 3a depicts the conservation technique for variables at the cell centers and boundary faces, which is termed the collocated technique. Figure 3b shows the segregated method of recording all the variable values in each face’s centroid. OpenFOAM stores the variables together, and the discretization procedures are addressed below.

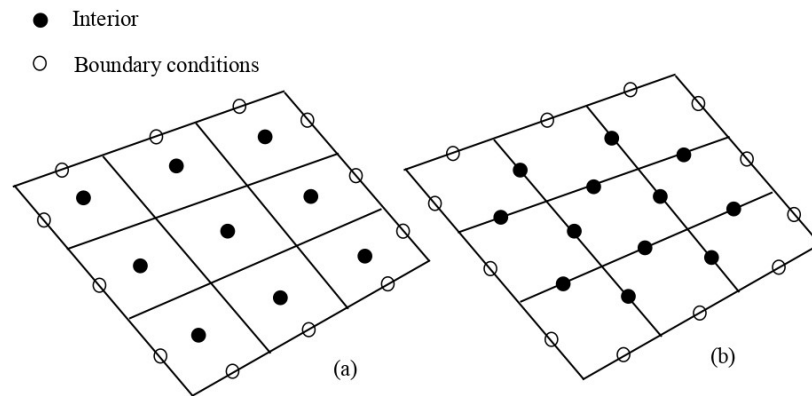


Figure 3. Options for storage of variables: (a) monolithic and (b) partitioned techniques.

For spatial-term discretization, the Gauss divergence theorem was applied, and the convection difference was utilized to calculate the face value from the cell centers. This approach aims to determine the quantity Φ on the face based on the magnitudes within the cell centers. Discretization techniques are confined to the nearest neighbors of the CV owing to the storage constraints on unstructured meshes. The central and upwind difference techniques have several variations; the OpenFOAM user guide lists all interpolation algorithms [31]. Diffusion-term discretization follows the convection-term discretization method. The SIMPLE (semi-implicit method for pressure-linked equations) and PISO (pressure implicit with splitting of operators) algorithms are used to solve pressure-linked equations. OpenFOAM uses SIMPLE for steady-state equations and PISO for transient equations [32]. In this study, we used the PISO and PIMPLE methods, which combine the PISO and SIMPLE algorithms. In OpenFOAM, FSI simulations were divided into monolithic and partitioned techniques. The robustness of the OpenFOAM algorithm can be utilized to obtain first-hand information on important parameters, which could be used in the design of many industrial applications [33–35]. The equation’s algorithms, solvers, and tolerances are monitored by using a dictionary located in the OpenFOAM system directory.

Figure 4 illustrates the sequential steps of the weak and strong coupling of the segregated technique from solid to liquid at each time step

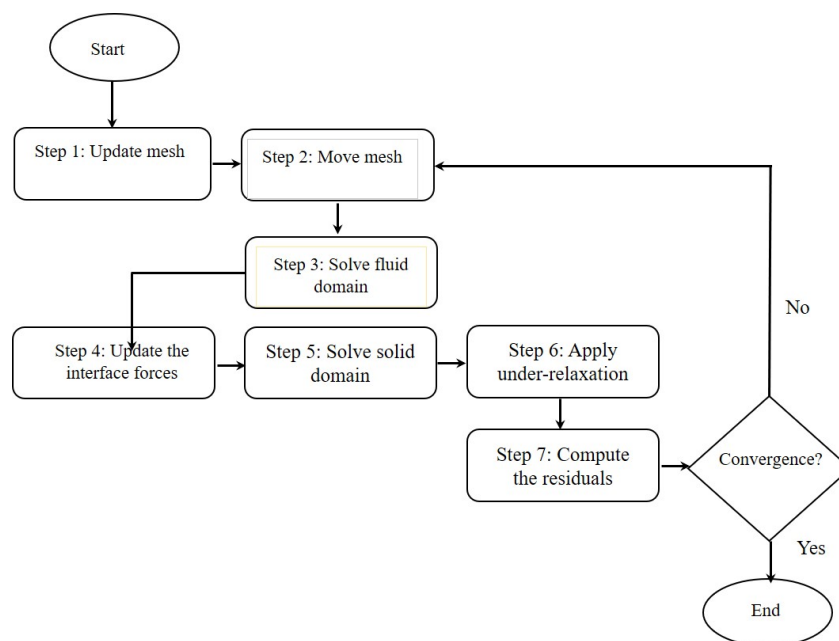


Figure 4. Solution processes of FSI from partitioned technique with weaker and stronger coupling.

In this case, the solver used was GAMG (geometric agglomerated algebraic multigrid), which requires the positive-definite diagonal matrix. In this solver, smoothing is an essential part of the multigrid method. The high frequency error on the current mesh can be reduced, as it solves for both symmetric and asymmetric matrices. The Gauss–Seidel smoothing scheme is applied in the solver, which means that the smoothing depends on the Gauss–Seidel method. For forced oscillation, the algorithm “pointDisplacement” in OpenFOAM is solely required to define the ratio f_n/f_v and the amplitude of oscillation (A/D). Furthermore, this algorithm utilizes two additional sub-algorithms, named “MeshDict” and “MotionU”. The prime objective is that movement can be achieved by moving either the cells themselves or the points. While the mesh can be moved by using either cell-based or point-based methods, the user has the option to perform motion computations based on velocity or the absolute/relative location. Moreover, a new corrected scheme was employed for face center discretization in the normal direction. This implemented scheme corrects the skewness and non-orthogonality of curved surfaces and boundaries.

The temporal integral was performed by using the explicit (forward Euler) method. The explicit procedure is unstable when the Courant number value is larger than 1. The Courant number (C_0) is defined as

$$C_0 = \frac{U\Delta t}{\Delta x},$$

where U is the flow velocity, and Δt and Δx are the mesh sizes for space and time, respectively. The input parameters of time step and output time interval must be adapted to reach a low Courant number and obtain an accurate solution, particularly for unsteady problems. When the flow velocity is increased, the simulation time step should be decreased in order to adjust the Courant number. In this analysis, the time step was chosen so that the Courant number remained less than 0.8.

4. Test Cases

4.1. VIV of Circular Cylinder

For the case of laminar flow conditions with $Re = 10^2$, a simulation of the VIV case in the cylindrical domain was performed. Structural damping was due to fluid viscosity since there was no cylinder motion to produce it.

Meshes for the motionless and dynamic cases are necessary because vortex shedding enables the movement of the cylinder. Here, the motion of the cylinder was tracked with a dynamic mesh. Therefore, a `dynamicMeshDict` file that specifies mesh motion that can be found under a constant directory was employed. All quantities, such as the pressure, speed, and location of the cylinder, must have specified initial and boundary conditions. The time increments must be modified by providing a Courant number of less than 0.2 in order to obtain correct results. The time increment was maintained as 0.001 for a simulation time of 100 s in the VIV case. This resulted in a small Courant number, and the corresponding predictions were ultimately reliable.

4.2. Computational Domain Schematics

In the first schematic, vortex-induced vibration was studied using both 1-DoF and 2-DoF. The cylinder could only move in the y -direction (transverse direction) in 1-DoF. The cylinder was assumed to vibrate freely in the x - and y -directions (by following in-line as well as crosswise paths) in the second case. Consequently, the following three distinct scenarios were examined in the latter:

- (i) In the first scenario, four springs with dampening effects were included. As a result, all springs applied four forces caused by spring effects, causing the damper to slow down. It is also important to remember that all springs were of the same size and that the cylinder could not spin on its axis. Nearly symmetrical stresses in the upper and lower regions of the cylinder were created by the fluid flow as it passed over

them. Technically, the point displacement file displays this scenario, which is for the 2-DoF structure.

- (ii) In the second scenario, more restrictions were added to the above, which forced the cylinder to travel only along the y -axis; this was termed the 1-DoF case.
- (iii) The third scenario had two springs and two dampers. As the cylinder moved along both the in-line and transverse paths, this also applied to the 2-DoF system. The density of the cylinder was set to 9.97 kg for each of the three cases, whereas the stiffness and damping values were $2 \text{ N} \cdot \text{s}/\text{m}$ and $4 \text{ N}/\text{m}$, respectively.

4.3. Mesh Generation

In OpenFOAM, the mesh can be generated in many ways. In this study, Gmsh software [31] was used for mesh generation. Then, gmshToFoam was used to write the mesh from the Gmsh form to the OpenFOAM form, and the results were stored in a separate directory. After generation, the mesh had 92,976 nodes and 45,940 elements. In this case, the static mesh was defined with Gmsh software, and its geometry is given in Figure 5. The mesh that was used in the above-defined VIV case is described in the following illustration. As seen in Figure 5, the mesh near the wall of the cylinder was built to be fine enough so that it would be easy to capture vortex shedding, which is important to generate cylinder motion. Additionally, in the other regions near the wall, the mesh was generated to be coarse in order to decrease the simulation time.

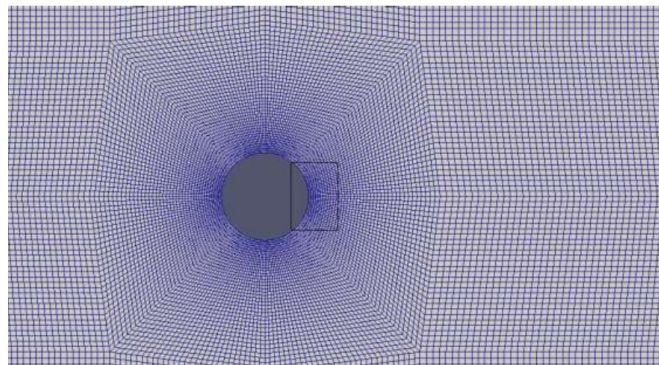


Figure 5. Circular cylinder mesh visualized in ParaView.

5. Results and Discussion

5.1. Freely Oscillating Cylindrical Structure

5.1.1. Discussion of Simulation Predictions of VIV for 1- and 2-DoF

The different flow regime predictions for a freely vibrating cylinder in the above-described situations are illustrated below.

For the first case, VIV was analyzed with 1-DoF and 2-DoF, with cylinder movement being considered along the y -axis for 1-DoF. In the second scenario, however, the cylinder could freely vibrate along both the x - and y -directions. Three distinct impacts were examined in these scenarios. For the first case, owing to the dampening impacts of the four springs, the forces acted along the four directions and, in turn, produced a decreasing effect. It is also worth noting that all the springs were of the same size and could not revolve about the axis. The fluid movement created almost symmetrical strains on the upper and lower edges of the cylinder as it passed over the structure. The second example had extra constraints with respect to the first, forcing the cylinder to only move in the y -direction. This was thus a one-dimensional case.

5.1.2. Drag and Lift Factors in the First Scenario

As shown in Figure 6, the drag factor nature for the 1-DoF structure was extremely close to that of the inert cylindrical structure; however, it was slightly different for the two-degrees-of-freedom system, notably between 10 and 20 s of simulation. Furthermore,

the drag factors for 1-DoF were larger than those for 2-DoF, but the lift factors for 1- and 2-DoF were nearly identical.

Nonetheless, a very small lag existed in reaction time, with the 2-DoF structure taking approximately 0.2 s longer to attain identical high amplitude values for drag and lift factors. This process is connected to the law according to which the 1-DoF case can only shift vertically, forcing an immediate reaction to any eddies formed along the wake region. At the same time, in the 2-DoF situation, the cylinder can also be pulled a little further along the path of the wake, causing a lag in the reaction to eddy forces. In other words, the lag is precisely proportional to the time taken by the springs to constrain the cylinder the rightmost when it begins to vibrate on a regular basis.

Compared with the 1-DoF example, the magnitude of the drag factor was reduced in the 2-DoF situation, and this could be connected with the supplementary DoF. In a similar manner, the lift factor had a small lower magnitude in the 2-DoF part owing to the pull by the cylinder alongside the flow and the shifting nearer the eddy trajectories.

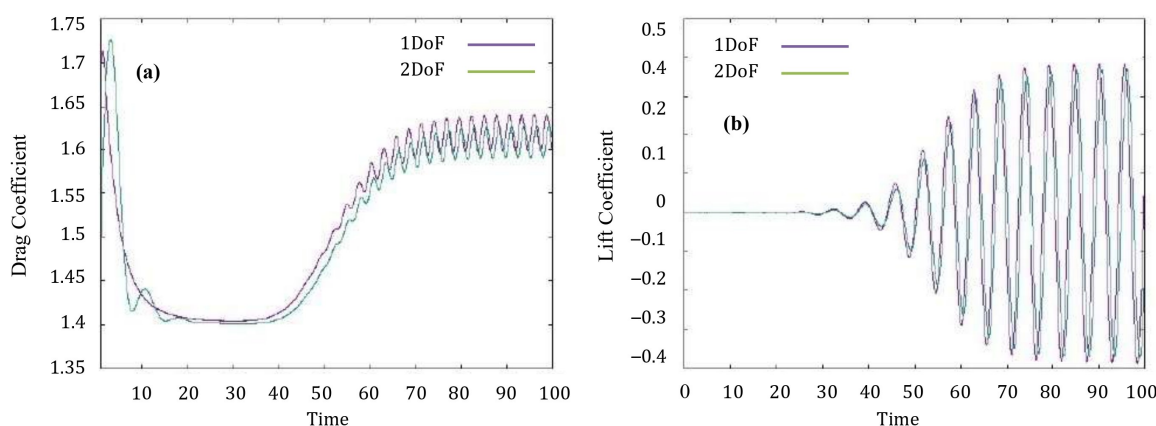


Figure 6. (a) Drag and (b) lift factors for 1 and 2 degrees of freedom.

5.1.3. Drag and Lift Factors in the Second Scenario

For scenario 2, Figure 7 displays the drag and the lift by comparing the predictions for the 1-DoF structure and the corresponding simulations for reduced damping and stiffness factors to unity. The predictions revealed that the drag and lift magnitudes for the actual case were relatively large compared with the reduced damping or spring rigidity.

To gain an understanding of this situation with double variants, the working nature of the spring and that of the damper must be known:

- (i) Force = stiffness × displacement. This indicates that the force caused by the spring varies linearly with the stiffness value.
- (ii) The movement of the damper is directly proportional to the velocity of its motion: Force = damping × velocity. This indicates that the damper generates greater force as a result of faster movement.

It is noteworthy that the forces exerted by the springs alter the cylinder movement. Specifically, the forces exerted by the springs alter the motion of the cylinder in response to the effects exerted by the fluid when the drag factor is estimated from the forces exerted on the cylinder. From these analyses, together with Figure 3, one can obtain a vivid understanding of the reductions in stiffness and damping as follows

1. The chosen three cases were assumed to be under-damped. This implies that the damper was not sufficient to halt oscillation; hence, all three had the same oscillation structure with the highest amplitude.
2. In addition, all the considered cases had similar drag factors until 30 s, provided that the movement paths were nearly identical during this initial period. The decrease in the drag factor must be equally associated with the generation of the first vortex and its release, with the next vortex successively originating and then being released.

3. The decreased damping contained less strength to react to the velocity force, resulting in the following:
 - 3.1. The larger drag factor from 30 s to nearly 63 s was caused by faster cylinder movement for similar forces acting on it, with the movement of the cylinder producing huge vortices and distorting the fluid.
 - 3.2. The smaller drag factor after 65 s was associated with a greater capability of the cylinder to weave and bob as eddies were created near the wake of the cylinder.
4. The decreased-stiffness scenario regularly contained a very small drag factor from the initial 30 s period, provided that it needed to be shifted for a longer distance for approximately the same forces to be exerted by the fluid on the cylinder surface.
5. In the lift case, the predictions were in line with those noticed when comparing the 1-DoF and 2-DoF cases having four springs, provided that the additional capability to shift the cylinder led to a small lift value, for the case where eddies could be created and discharged with small dragging efforts.
6. In the last analogy, it could be observed that a decrement in stiffness created smaller amplitudes of the drag and lift after the initial 30 s period.

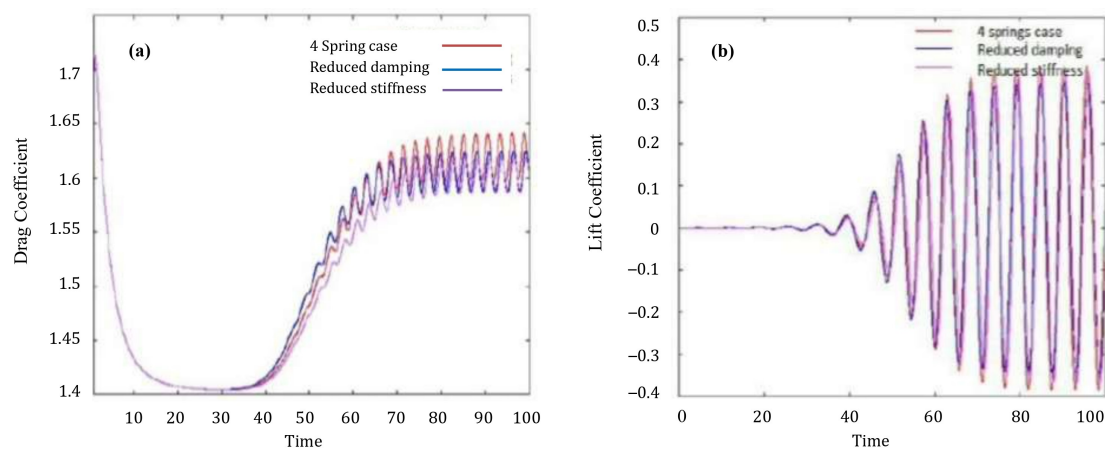


Figure 7. (a) Drag and (b) lift factors for 1 degree of freedom.

5.1.4. Drag and Lift Factors in the Third Scenario

By comparing the predictions obtained for the case of 1-DoF, the drag factors of the 2-DoF structure (case 1) revealed distinct behavior during the initial 30 s period. As noticed earlier for the variations in damping and stiffness for the 1-DoF situation, for the initial period, the following observations are noted:

1. The decreased damping led to quicker motion, which clearly indicates a rapid response interval for the cylinder to shift along the vortices at a relatively higher rate compared with the remaining two types. Therefore, the greatest amplitudes in the first 30 s were greater/smaller compared with the benchmark 2-DoF situation.
2. The decreased stiffness enabled the cylinder to shift away and create tiny vortices with lower intensity compared with the previous types.

After 30 s, the predictions were similar to the variants observed in the 1-DoF case, as follows:

1. The decreased damping permitted a lower drag factor compared with the actual state;
2. The lowest drag factor was produced with reduced stiffness;
3. The two variants had almost similar frequency as observed in the reference 2-DoF situation.

With regard to lift, the predictions were nearly the same, particularly for the decreased-stiffness and -damping situations. In general, the 1-DoF and 2-DoF systems revealed larger amplitudes for the actual case compared with the decreased spring stiffness because of the

similar phenomenon relative to these factors, which leads to the elimination of vibration after some time (see Figures 7 and 8).

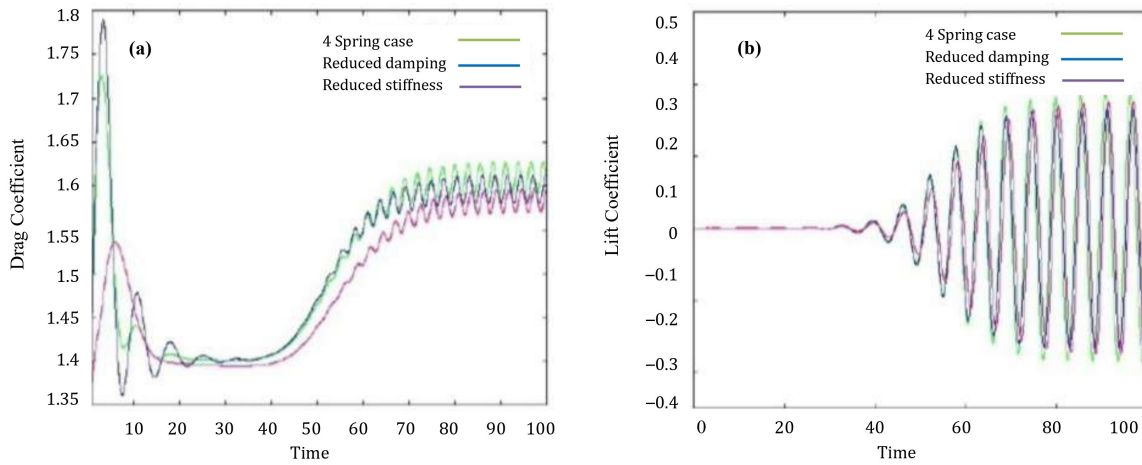


Figure 8. (a) Drag and (b) lift factors for 2 degrees of freedom.

5.1.5. Drag and Lift Factors in Reduced-Damping Scenario

The drag factor results for the reduced-damping case reveal a significant variation between the 1-DoF and 2-DoF cases during the initial prediction period, as illustrated in Figure 9. The drag factor for 1-DoF is similar to the reference 1-DoF situation. However, the 2-DoF case reveals a structure with greater oscillation until approximately 35 s of the solution period. This could be due to reduced damping, which permits the rapid reaction of the springs. The following conclusions were drawn:

1. For uniform periodic oscillation in the two cases, the prediction of 1-DoF revealed a stronger drag factor compared with the respective reference cases.
2. With regard to the lift, the predictions were nearly the same as the previously obtained results.

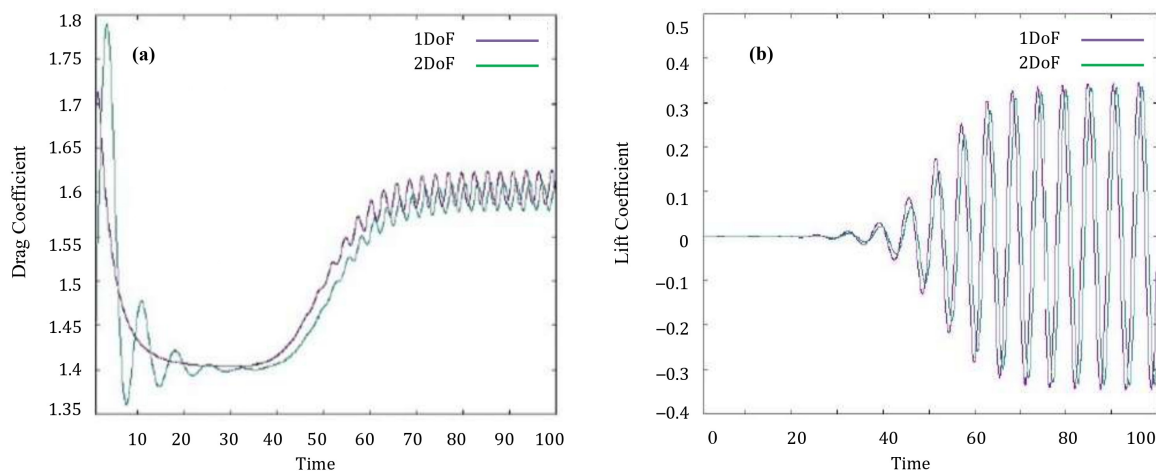


Figure 9. (a) Drag and (b) lift factors for reduced-damping scenario with 1 and 2 degrees of freedom.

5.1.6. Drag and Lift Factors in Scenario with Reduced Spring Stiffness and One and Two Degrees of Freedom

The 1-DoF drag predictions revealed the largest magnitudes for the entire solution period, and the lift predictions revealed relatively higher values for 1-DoF. From the points of view of lower energy and interference with fluid motion, this could be the best structure to use, if further optimization is not possible. Particularly, this is due to the lift working conditions and is similar to the other cases, as evidenced in Figure 10.

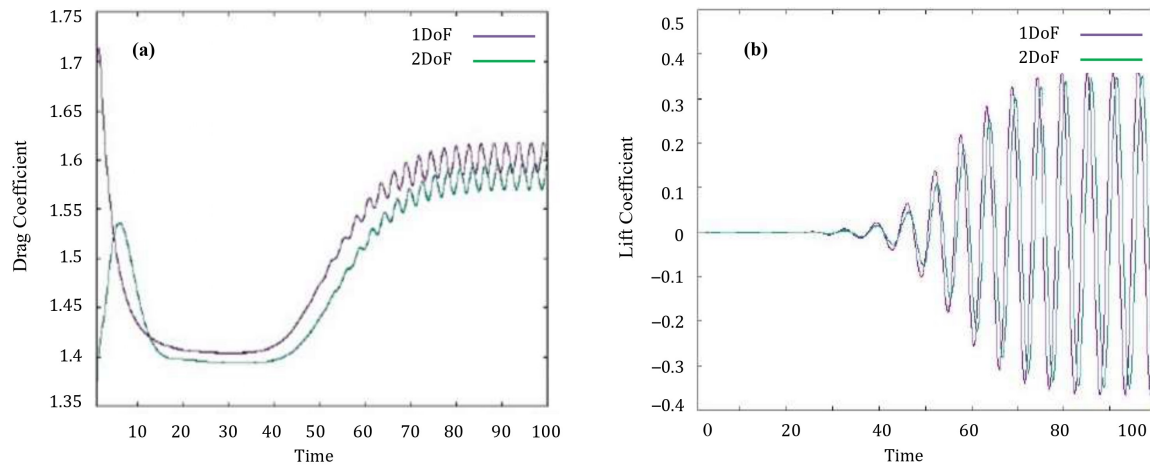


Figure 10. (a) Drag and (b) lift factors for reduced spring stiffness case with 1 and 2 degrees of freedom.

5.1.7. Lift and Drag Factors for 2-DoF System with Four Springs and Two Springs plus Two Dampers

Figure 11 portrays the comparison of predictions of the 2-DoF systems (case 1 with four springs fixed to the cylinder and case 3 with two springs and two dampers).

The drag predictions revealed considerably different results in both cases. For the four-spring case, the drag factor decreased significantly from around 1.73 at 3 s to 1.4 at 40 s (approximately) and later increased uniformly until approximately 70 s of the solution period to initiate a similar oscillating behavior. However, the 2-DoF situation having two springs and two dampers assumed similar oscillating behavior from 30 s of the solution period, rather than 70 s. Further, the lift factor for case 1 had zero lift until approximately 40 s; however, the lift predictions revealed oscillation from the beginning until the end of the simulation period, which could have been due to the dampers for the other situation. However, during the last stage of the simulation period, the lift factors in both cases were similar. When restructuring the drag paths in both cases, the observations given below were noted:

1. The dissimilar nature of the damper/spring structure could be noticed in the respective plot from the 25–30 s mark. This behavior could have been due to the non-alignment of dampers and springs, causing the cylinder to shift faster, based on the position of the cylinder.
2. The greatest amplitude of the drag factor was small in case 3 compared with the predictions in other cases.
3. The reduced damping led to a shorter reaction time and was systematically identified, provided it took approximately 40 s less to attain the periodic working area.

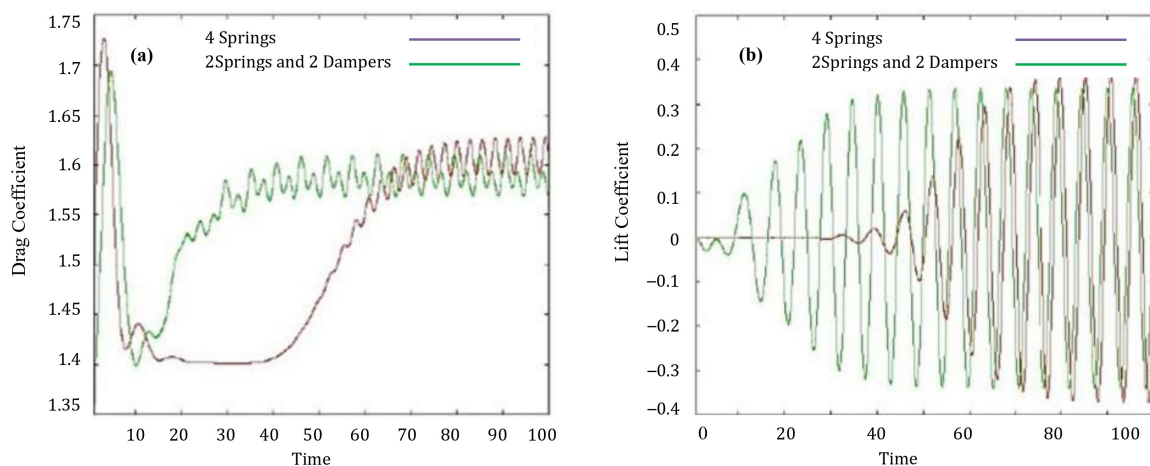


Figure 11. (a) Drag and (b) lift factors for 2 degrees of freedom.

5.2. Forced Oscillating Cylindrical Structure

The current sample case was estimated by using identical Reynolds numbers ($Re = 100$). Figures 12 and 13 display the simulation findings for the forced coefficients. The calculated natural frequency (f_n) was 0.482Hz. This scenario exhibited a moderately elevated upward movement, as depicted in Figure 13. Owing to the highly distorted mesh, the simulation was initially motionless. This suggests that the cylinder was in a state of resonance. The frequency ratio ($Fr = f_n/fv$) is defined as the ratio between the natural frequency of the cylinder (f_n) and the vortex shedding frequency of the static cylinder (fv). The Strouhal number, determined as 0.167, corresponded to a vortex shedding frequency (fv) of 0.167Hz. The value of the natural frequency, f_n , was 0.482Hz. The amplitude of the cylinder reached its maximum value when the ratio of the natural frequency (f_n) to the forced vibration frequency (fv) was 2.87.

These two predictions provide insights into the generation and release of vortices as the cylinder undergoes vertical motion. To draw this conclusion, the following observations were made:

1. Figure 12 demonstrates that the highest values of the drag coefficient align with the lowest and highest points of the lift, while the lowest values of the drag coefficient corresponded to the locations where the lift was zero.
2. Furthermore, Figure 13 demonstrates a clear correlation between the peaks of the lift and increases in the movement of the cylinder. This indicates that the highest dislocation values corresponded to the highest values of the drag factor. The zero-lift locations corresponded to the instances when the cylinder crossed the central axis during forced oscillation.

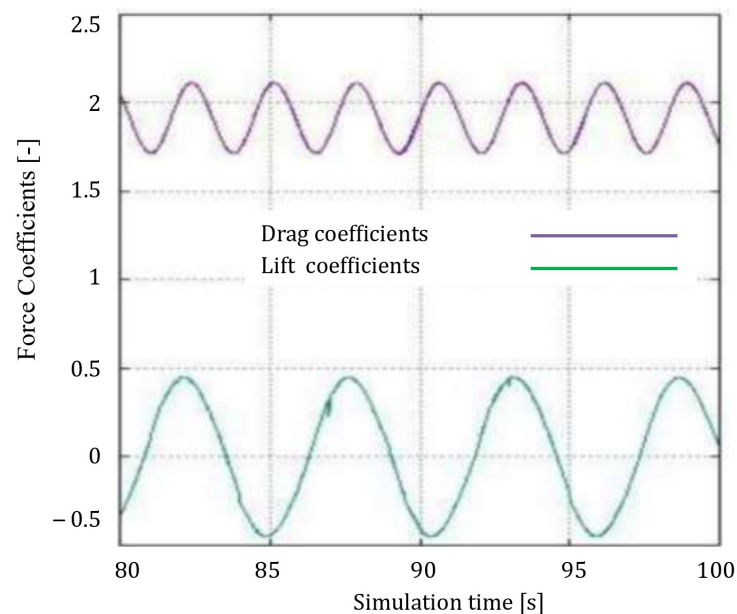


Figure 12. Force coefficients of forced oscillation cylinder case under laminar flow with $Re = 100$.

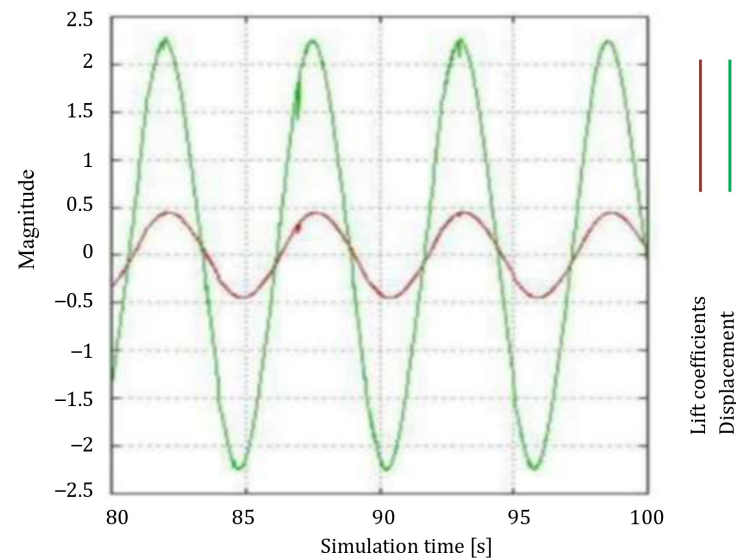


Figure 13. Vertical displacement and lift coefficient time histories of the forced oscillation case.

6. Conclusions

From the extensive VIV numerical experiments performed, the following significant findings are reported:

1. Damping and stiffness impacted the behavior of the cylinder along with the flow, and there were important noticeable variations in the response time and starting speed in which the process responded to the flow; this was also true in the case in which the constant periodic oscillation was stabilized.
2. For the 2-DoF scenario, during the initial phase, a decrease in damping led to a significantly high drag coefficient, whereas a decrease in stiffness decreased the maximum drag coefficient.
3. The behavior of the cylinder was significantly altered by the linear nature of the springs and dampers. In particular, the cylinder response period and the drag factor were significantly affected by the stiffness and damping factors.
4. If the mechanism is intended to include more drag, then the dampers should be kept at a minimum or withdrawn for stiff springs. If the mechanism requires minimum drag, moderate damping magnitudes are required with fairly relaxed springs.
5. At the point of zero lift, when the forces forming the vortex were in equilibrium, which occurred at approximately 10s, the wake in close proximity to the cylinder was nearly parallel to the fluid flow, which moved from left to right.
6. The drag and lift coefficients reach their greatest values when (a) a domain of high-velocity flow passes over top of the cylinder while it is in the upper position or (b) when a high-velocity flow is directed towards the cylinder while it is in the lower position, which was noted at around 30 s in this study.
7. The observed peaks in the drag and lift coefficients align with the expected behavior of wings and airfoils under identical operating conditions, specifically when comparing the maximum values for wings/airfoils.
8. The current analysis was limited to $Re = 100$, and the FSI and VIV analyses were confined to a flow over a cylinder. This work could be extended to include higher Reynolds numbers and objects with other shapes. Because of research limitations, turbulence modeling was not used in this study.

Author Contributions: Conceptualization, methodology, software, original draft preparation, M.S.A.M.; review and editing, plagiarism reduction, M.S.; project administration, funding acquisition, C.A.; preparation of graphs, literature review, B.V.P. All authors have read and agreed to the published version of the manuscript.

Funding: This research study was funded by University of Technology and Applied Sciences, Ibri, through Internal Funding Grant with grant number IRFP-IBRI-24-02, and the APC was funded through this project grant.

Data Availability Statement: The original contributions presented in the study are included in the article, further inquiries can be directed to the corresponding author.

Acknowledgments: The authors acknowledge the support and encouragement from University of Technology and Applied Sciences(UTAS)-Ibri, Oman, under Internal Research Funding project No. IRFP-IBRI-24-02.

Conflicts of Interest: The authors declare no conflicts of interest.

References

- Anagnostopoulos, P. Numerical investigation of response and wake characteristics of a vortex-excited cylinder in a uniform stream. *J. Fluids Struct.* **1994**, *8*, 367–390. [[CrossRef](#)]
- Anagnostopoulos, P. Numerical study of flow past a cylinder excited transversely to the incident stream. Part I: Look-in zone, hydrodynamic forces and wake geometry. *J. Fluids Struct.* **2000**, *14*, 819–851. [[CrossRef](#)]
- Govardhan, R.; Williamson, C. Modes of vortex formation and frequency response of a freely vibrating cylinder. *J. Fluid Mech.* **2000**, *420*, 85–130. [[CrossRef](#)]
- Williamson, C.H.K.; Govardhan, R. Vortex-induced vibrations. *Annu. Rev. Fluid Mech.* **2004**, *36*, 413–455. [[CrossRef](#)]
- Williamson, C.; Jauvtis, N. A high-amplitude 2T mode of vortex-induced vibration for a light body in motion. *Eur. J. Mech. B/Fluids* **2004**, *23*, 107–114. [[CrossRef](#)]
- Bourguet, R.; Karniadakis, G.; Triantafyllou, M. Vortex-induced vibrations of a long flexible cylinder in shear flow. *J. Fluid Mech.* **2011**, *677*, 342–382. [[CrossRef](#)]
- Mittal, S. Excitation of shear layer instability in flow past a cylinder at low Reynolds number. *Int. J. Numer. Methods Fluids* **2005**, *49*, 1147–1167. [[CrossRef](#)]
- Jung, J.H.; Jeong, K.L.; Gill, J.H.; Jung, D. Large eddy simulation of free motion of marine riser using OpenFOAM. *J. Ocean. Eng. Technol.* **2019**, *33*, 387–393. [[CrossRef](#)]
- Leong, C.; Wei, T. Two-degree-of-freedom vortex-induced vibration of a pivoted cylinder below critical mass ratio. *Proc. R. Soc. A Math. Phys. Eng. Sci.* **2008**, *464*, 2907–2927. [[CrossRef](#)]
- Srinil, N.; Zanganeh, H.; Day, A. Two-degree-of-freedom VIV of circular cylinder with variable natural frequency ratio: Experimental and numerical investigations. *Ocean. Eng.* **2013**, *73*, 179–194.
- Xie, F.; Deng, J.; Xiao, Q.; Zheng, Y. A numerical simulation of VIV on a flexible circular cylinder. *Fluid Dyn. Res.* **2012**, *44*, 045508. [[CrossRef](#)]
- Xiao, Z.J.; Yang, S.H.; Yu, C.; Zhang, Z.; Sun, L.; Lai, J.; Huang, Y.P. Effects of cavitation on vortex-induced vibration of a flexible circular cylinder simulated by fluid-structure interaction method. *J. Hydrodyn.* **2022**, *34*, 499–509. [[CrossRef](#)]
- Deng, D.; Zhao, W.; Wan, D. Numerical study of vortex-induced vibration of a flexible cylinder with large aspect ratios in oscillatory flows. *Ocean. Eng.* **2021**, *238*, 109730. [[CrossRef](#)]
- Raghavan, K.; Bernitsas, M. Experimental investigation of Reynolds number effect on vortex induced vibration of rigid circular cylinder on elastic supports. *Ocean. Eng.* **2011**, *38*, 719–731. [[CrossRef](#)]
- Koubogiannis, D.G.; Benetatos, M.V.N. Numerical Assessment of Flow Energy Harvesting Potential in a Micro-Channel. *Fluids* **2023**, *8*, 222. [[CrossRef](#)]
- Xiao, D.; Hao, Z.; Zhou, T.; Zhu, H. Experimental Studies on Vortex-Induced Vibration of a Piggyback Pipeline. *Fluids* **2024**, *9*, 39. [[CrossRef](#)]
- Gonçalves, R.A.; Teixeira, P.R.D.F.; Didier, E.L. Numerical simulations of low Reynolds number flows past elastically mounted cylinder. *Eng. Térmica (Therm. Eng.)* **2012**, *11*, 61–67. [[CrossRef](#)]
- Li, M.; Bernitsas, C.; Jing, G.; Hai, S. Hydrokinetic Power Conversion Using Vortex-Induced Oscillation with Cubic Restoring Force. *Energies* **2020**, *13*, 3283. [[CrossRef](#)]
- Zhang, D.; Feng, L.; Yang, H.; Li, T.; Sun, H. Vortex-Induced Vibration Characteristics of a PTC Cylinder with a Free Surface Effect. *Energies* **2020**, *13*, 907. [[CrossRef](#)]
- Narváez, G.F.; Schettini, E.B.; Silvestrini, J.H. Numerical simulation of flow-induced vibration of two cylinders elastically mounted in tandem by immersed moving boundary method. *Appl. Math. Model.* **2020**, *77*, 1331–1347. [[CrossRef](#)]
- Wu, Y.; Lien, F.-S.; Yee, E.; Chen, G. Numerical Investigation of Flow-Induced Vibration for Cylinder-Plate Assembly at low Reynolds Number. *Fluids* **2023**, *8*, 118. [[CrossRef](#)]
- Sciortino, G.; Lombardi, V.; Prestininzi, P. Modelling of Cantilever-Based Flow Energy Harvesters Featuring C-Shaped Vibration Inducers: The Role of the Fluid/Beam Interaction. *Appl. Sci.* **2023**, *13*, 416. [[CrossRef](#)]
- Michna, J.; Rogowski, K. Numerical study of the effect of the Reynolds number and the turbulence intensity on the performance of the NACA 0018 Airfoil at the low Reynolds number regime. *Processes* **2022**, *10*, 1004. [[CrossRef](#)]

24. Placzek, A.; Sigrist, J.; Hamdouni, A. Numerical simulation of an oscillating cylinder in a cross-flow at low Reynolds number: Forced and free oscillations. *Comput. Fluids* **2009**, *38*, 80–100. [[CrossRef](#)]
25. Bearman, P.W. Understanding and predicting vortex-induced vibrations. *J. Fluid Mech.* **2009**, *634*, 1–4. [[CrossRef](#)]
26. Bearman, P.W. Circular cylinder wakes and vortex-induced vibrations. *J. Fluids Struct.* **2011**, *27*, 648–658. [[CrossRef](#)]
27. Schafer, F.; Uffinger, T.; Becker, S.; Grabinger, J.; Kaltenbacher, M. Fluid-structure interaction and computational aeroacoustics of the flow past a thin flexible structure. *J. Acoust. Soc. Am.* **2008**, *123*, 3570–3575. [[CrossRef](#)]
28. Patnana, V.K.; Bharti, R.P.; Chhabra, R.P. Two-dimensional unsteady flow of power-law fluids over a cylinder. *Chem. Eng. Sci.* **2009**, *64*, 2978–2999. [[CrossRef](#)]
29. Hirsch, C. *Numerical Computation of Internal and External Flows: The Fundamentals of Computational Fluid Dynamics*; Butterworth-Heinemann: Oxford, UK, 2007.
30. Muzafferija, S. Adaptive Finite Volume Method for Flow Prediction Using Unstructured Meshes and Multigrid Approach. Ph.D. Thesis, Imperial College, University of London, London, UK, 1994.
31. OpenFOAM Foundation. *OpenFOAM User Guide*; Version 2.2.2; OpenFOAM Foundation: London, UK, 2013.
32. Maric, T.; Hopken, J.; Mooney, K. *The OpenFOAM Technology Primer*; Sourceflux UG (haftungsbeschränkt): Duisburg, Germany, 2014.
33. Yakush, S.E.; Sivakov, N.S.; Melikhov, O.I.; Melikhov, V.I. Numerical Modeling of Water Jet Plunging in Molten Heavy Metal Pool. *Mathematics* **2024**, *12*, 12. [[CrossRef](#)]
34. Ke, L.; Wang, Q. Numerical Simulation of the Stability of Low Viscosity Ratio Viscoelastic Lid-Driven Cavity Flow Based on the Log-Conformation Representation (LCR) Algorithm. *Mathematics* **2024**, *12*, 430. [[CrossRef](#)]
35. Aghajanzpour, A.; Khatibi, S. Numerical Study of Velocity and Mixture Fraction Fields in a Turbulent Non-Reacting Propane Jet Flow Issuing into Parallel Co-Flowing Air in Isothermal Condition through OpenFOAM. *AppliedMath* **2023**, *3*, 468–496. [[CrossRef](#)]

Disclaimer/Publisher’s Note: The statements, opinions and data contained in all publications are solely those of the individual author(s) and contributor(s) and not of MDPI and/or the editor(s). MDPI and/or the editor(s) disclaim responsibility for any injury to people or property resulting from any ideas, methods, instructions or products referred to in the content.